

Modeling seismic attenuation and dispersion in partially saturated rocks based on fluid distribution from computed tomography scans

Jing Ba¹, Haojie Che¹, Chao Sun², Lin Zhang¹, and José M. Carcione³

ABSTRACT

The anelastic properties of seismic waves (attenuation and velocity dispersion) in partially saturated rocks depend on the spatial distribution of pore fluids. We map the fluid distributions in three sections of a limestone core sample with X-ray computed tomography (CT) scans and obtain the radii and volume fractions of the gas patches. These statistical data are input into an infinituple-porosity model with partial saturation, the results of which are compared with the forced oscillation (from 0.004 to 100 Hz) and ultrasonic (1 MHz) measurements, and the results of other approaches (the fractal model, the continuous random media model, and the finite-element method). The anelastic properties indicate significant differences among different sections due to fluid distribution. We find that it is possible to effectively characterize seismic anelasticity in a partially saturated limestone by using actual fluid distributions from CT scans and an appropriate petroelastic model. The agreement between the theory and the experiment proves the validity of our approach.

INTRODUCTION

Wave-induced fluid flow (WIFF) in partially saturated rocks is considered one of the main causes of anelasticity (attenuation and velocity dispersion) (Pride et al., 2004; Müller et al., 2010; Ba et al., 2013, 2019; Solazzi et al., 2019; Guo and Gurevich, 2020; Kumar et al., 2022). These effects depend on the saturation, distribution, and physical properties of the pore fluid. Differences in fluid properties, heterogeneity on the rock frame, and other factors lead to attenuation

due to mesoscopic flow, with scales much smaller than the seismic wavelength but larger than the pore/grain size.

Previous theoretical and experimental studies have shown that WIFF causes significant anelasticity (White et al., 1975; Murphy, 1982; Carcione et al., 2003; Carcione and Picotti, 2006; Ba et al., 2008; Sharma and Kumar, 2011; Deng et al., 2012; Wang, 2016; Ba et al., 2017; Wu et al., 2020; Kumar et al., 2023, 2024). White (1975) introduces the first model based on spherical fluid patches, and Dutta and Seriff (1979) reformulate the White model based on the Biot theory. Johnson (2001) extends the White model to patches of arbitrary shapes. Müller and Gurevich (2004) propose a model assuming random fluid distributions. Liu et al. (2010) analyze the effects of different fluids on the anelastic properties. Ba et al. (2011, 2014) derive the Biot-Rayleigh equations for wave propagation in rocks with double porosity. Zhang et al. (2021) combine the differential effective medium theory and Biot-Rayleigh theory to derive an infinituple-porosity model (IPM), and Zhang et al. (2022) extend this model to partial saturation based on the fractal patches, hereafter referred to as the IPM with partial saturation (IPMPS) model. Wu et al. (2021) develop a model for partially saturated media by combining the micro-scale squirt-flow and the mesoscale patchy-saturation theories.

Computed tomography (CT) scans are widely adopted to map the fluid spatial distribution in real rocks. Cadoret et al. (1995) perform experiments on partially saturated limestone samples using drying and depressurization methods, wherein CT scanning was adopted to image the fluid distribution. They find that the fluid distribution under depressurization conditions is more uniform, whereas drying leads to heterogeneous distributions. Toms-Stewart et al. (2009) compute the Debye correlation length based on CT scans and observe that, with increasing gas saturation, the length exhibits a nearly linear decrease. This indicates that the correlation length is highly sensitive to gas saturation and can serve as a key parameter for quantifying changes in

Manuscript received by the Editor 18 May 2024; revised manuscript received 1 December 2024; published ahead of production 17 February 2025; published online 22 April 2025.

¹Hohai University, School of Earth Sciences and Engineering, Nanjing, China. E-mail: jba@hhu.edu.cn; chehaojie@hhu.edu.cn; zlin@hhu.edu.cn (corresponding author).

²China University of Mining and Technology, College of Resources and Geoscience, Xuzhou, China. E-mail: sunchao@cumt.edu.cn.

³Hohai University, School of Earth Sciences and Engineering, Nanjing, China and National Institute of Oceanography and Applied Geophysics — OGS, Trieste, Italy. E-mail: jose.carcione@gmail.com.

© 2025 Society of Exploration Geophysicists. All rights reserved.

gas saturation. Qi et al. (2014) extend the random patchy-saturation model to study capillary pressure effects on fluid patches, with the fluid distribution obtained using CT images. Based on the CT scans measured by Cadoret et al. (1995), Kobayashi and Mavko (2016) extend the dynamic equivalent-medium approach to partially saturated media by introducing correlation lengths varying with the saturation. This method can predict the anelasticity of P waves quite well. Chapman et al. (2021) perform depressurization experiments to induce the exsolution of carbon dioxide from the water in the Berea sandstone samples and characterize the fluid distribution with CT scans as input to calculate the anelasticity. Their numerical solution is consistent with laboratory experiments. Sun et al. (2022, 2023a) use a finite-element method combined with CT scans to determine P-wave anelasticity. Their simulations agree with the experimental results.

In previous studies (e.g., Carcione and Picotti, 2006; Zhang et al., 2015), the patch size could be assumed in modeling the wave responses for a patchy-saturated rock. Here, we obtain CT scans of the core samples to map the fluid distribution, and the patch radii and volume fractions are used as inputs for the IPMPS model. The results are then validated against the experimental data. Figure 1 shows the workflow for comparing theoretical modeling with experimental results.

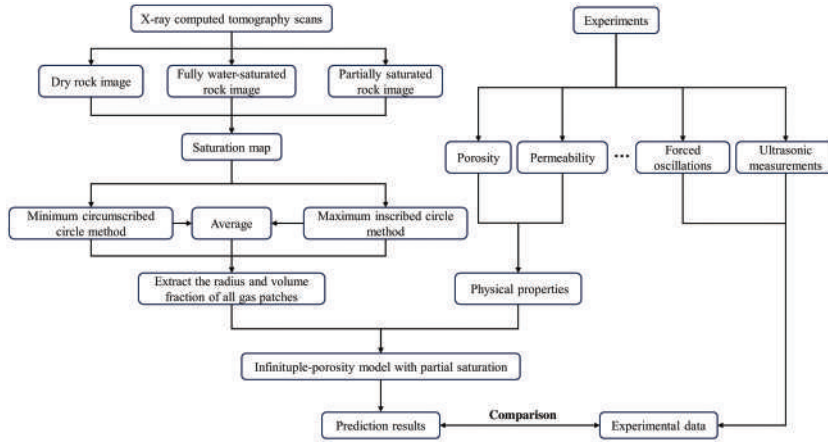


Figure 1. Workflow to compare the theoretical and experimental results.

Table 1. Physical properties of the Indiana limestone (from Sun et al., 2022).

	Indiana limestone	Air	Water
Grain bulk modulus (GPa)	$K_s = 77$		
Bulk modulus (GPa)	$K_b = 25$	$K_f^l = 1 \times 10^{-4}$	$K_f^H = 2.25$
Shear modulus (GPa)	$G_b = 15.2$		
Density (g/cm^3)	$\rho_s = 2.3692$	$\rho_f^l = 0.001$	$\rho_f^H = 1$
Viscosity (Pa·s)		$\eta_f^l = 2 \times 10^{-5}$	$\eta_f^H = 10^{-3}$
Porosity (%)	$\phi = 10.8$		
Permeability (m^2)	$\kappa = 2 \times 10^{-17}$		

Note: The dry-rock bulk (K_b) and shear (G_b) moduli of Indiana limestone were measured at the confining pressure of 5 MPa.

CT SCANS FOR SATURATION MAPS

Samples and experiments

The sample was taken from Indiana limestone, as described by Borgomano et al. (2019) and other works (e.g., Michalopoulos and Triandafilidis, 1976; Hart and Wang, 1995; Vajdova et al., 2004; Zhu et al., 2010; Ji et al., 2012). All the experimental data (forced oscillations, ultrasonic measurements, and CT scan data) in this paper were provided by Sun et al. (2022). The physical properties are provided in Table 1. The porosity was measured by the triple-weight method, and the permeability was measured by the steady state fluid flow under water saturation (Borgomano et al., 2019). The CT scanned volume had a diameter of 40 mm and a height of 38.4 mm, with a voxel size of $0.022 \text{ mm} \times 0.022 \text{ mm} \times 0.022 \text{ mm}$. The images in different saturation states are shown in Figure 2. Figure 3a shows the spatial location of the different sections. The statistical analysis of the variation in porosity with the volume in 3D digital cores has determined the representative elementary volume (REV), as characterized by Bear (1972). As shown in Figure 3b, we consider 10 test points within the 3D digital core and analyze the trend of porosity variation with increasing pixel count at these points. At a pixel count of 150, the porosity is stable and approaches the sample (10.8%). The acceptable REV scale is approximately 3.3 mm (a pixel count of 150 and a pixel size of 0.022 mm).

Reconstruction of the saturation map

Following Toms-Stewart et al. (2009), the pixels of the dry-rock image have the following values:

$$CT_{\text{dry}} \approx (1 - \phi)CT_{\text{grain}} + \phi CT_{\text{air}}, \quad (1)$$

where ϕ is the porosity and CT_{grain} and CT_{air} correspond to the grains and air-filled pore spaces, respectively. At full water saturation, we have

$$CT_{\text{fullsat}} \approx (1 - \phi)CT_{\text{grain}} + \phi CT_{\text{water}}. \quad (2)$$

In drainage, the gas in the pore space is air. For partial saturation, we have

$$CT_{\text{partsat}} \approx (1 - \phi)CT_{\text{grain}} + \phi(v_1 CT_{\text{water}} + v_2 CT_{\text{air}}), \quad (3)$$

where v_1 and v_2 are the percentages of water and air in the pore spaces, respectively.

Equations 1–3 lead to errors at the grain/pore interfaces that are negligible, according to Ketcham and Carlson (2001), because these interfaces rotate randomly relative to the plane of the scan. In general, the CT value does not change significantly with the relative proportion of gas to water in the pore space. The CT value that changes with gas saturation is much smaller than the CT value of the rock skeleton.

To effectively determine the gas distribution, we use the approach of Cadoret et al. (1995) to construct a gas-saturation map. First, we measure the CT images at different saturation states. Then, the porosity map is obtained by subtracting the full water-saturation image from the dry-rock image, and the gas content map is obtained by subtracting the partial water-saturation image from the full

water-saturation one. Eventually, the gas-saturation map is obtained by dividing the gas content map by the porosity map.

The pixels of the three maps have the following values:

$$CT_{\text{por}} = \phi(CT_{\text{air}} - CT_{\text{water}}), \quad (4)$$

$$CT_{\text{aircont}} = \phi v_2(CT_{\text{water}} - CT_{\text{air}}), \quad (5)$$

$$CT_{\text{airsat}} = -v_2. \quad (6)$$

In the calculation, the pixel size is coarsened from 0.022 to 0.176 mm. Coarsening is applied to obtain a representative elemental volume in which porosity and gas saturation are determined and to reduce errors in these properties (Chapman et al., 2021).

Statistical characteristics of the gas patches

The gas-saturation map obtained is shown in Figure 4, where small gas patches can be seen. These patches do not represent the actual fluid distribution but rather the noise generated during the experiment, as it is not guaranteed that the spatial location of the sample after each scan is entirely consistent with the previous one. Cadoret et al. (1995) also discuss this noise.

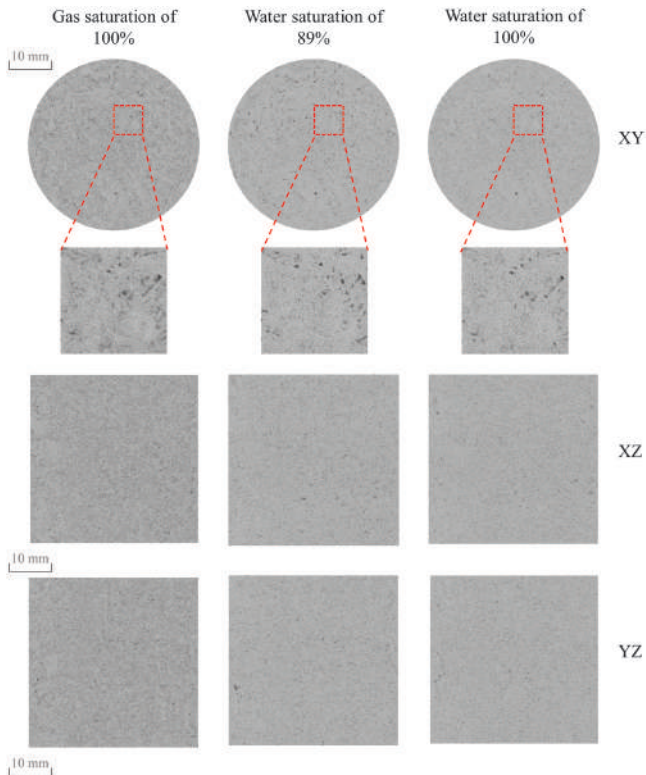


Figure 2. The CT scan images along different sections with saturations, extracted based on the CT data of Sun et al. (2022). Here, XY, XZ, and YZ denote the core sections (the black: the pores, where gas exhibits an even darker color compared with water, and the gray: the grains).

To eliminate the noise, adaptive filtering is applied to the gas-saturation map. The adaptive filter is more selective than a comparable linear filter, preserving the edges and other high-frequency parts of an image. This involves binary segmentation using a global threshold to filter out the noise. The image is then converted to a binary matrix. The binary gas-saturation map, as shown in Figure 5, includes water-saturated regions (in blue) and gas-saturated regions (in orange). The binary map provides a visual representation of the distribution of the gas patches. In the XY section, the distribution of the patches is more uniform and their size is much smaller than in the XZ and YZ sections. Differences in the spatial distribution of pore structures (i.e., the pores and cracks) and the density of gas, which is obviously less than that of water, can lead to discrepancies between the patch sizes obtained from the XY section and those obtained from the XZ and YZ sections, which may be the reason why the patch size obtained from the XY section is smaller than those obtained from the XZ and YZ sections.

We perform a statistical analysis of the gas patch size for the three different sections. By finding the smallest circumscribed circle and the largest inscribed circle for the irregular shape, we obtain the circumradius and inradius of the gas patch, and the average radius is then obtained as the average of the two values. The volume fraction is determined by counting the percentage of the individual gas

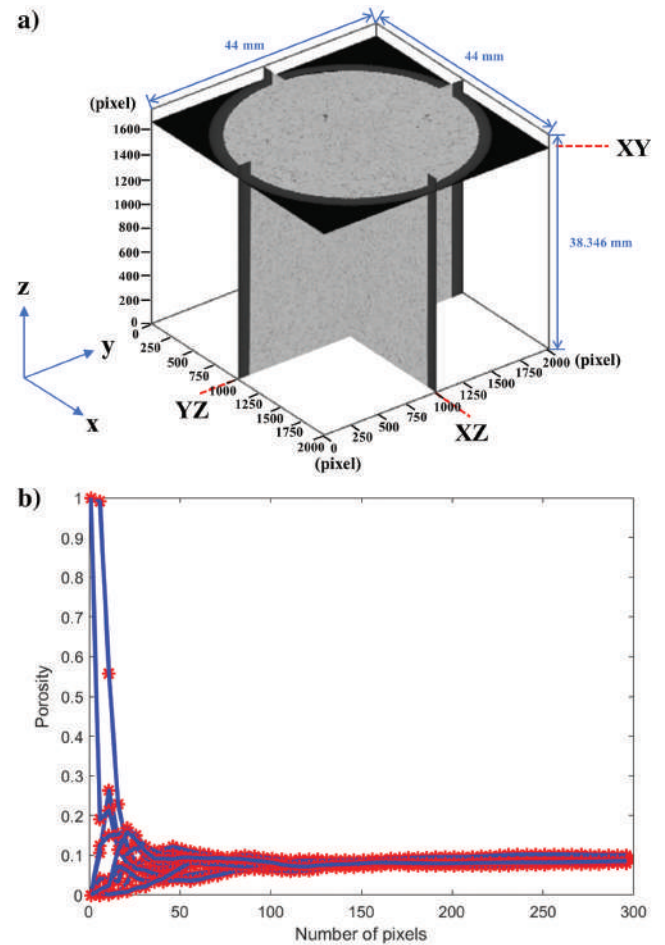


Figure 3. (a) The spatial locations of the three sections and (b) the relationship between the REV size and porosity.

patch in the binary map shown in Figure 5. Thus, we obtain the data for the three sets of radii (r) and volume fraction (v).

Figure 6 shows the range of the radius distribution resulting from the statistical analysis of the sections. It is noticeable that the number of bins for the inradius is smaller, and the frequency is higher for the circumradius. This discrepancy is attributed to the coarsening effect. The histogram for the XY section has an overall exponential distribution. The number of small radii (circumradius <0.24 mm,

average radius <0.2 mm, and inradius <0.17 mm) accounts for a large proportion of all the patches. As the radius increases, the proportion gradually decreases. In contrast, the histograms for the XZ and YZ sections are similar. The number of large radii (circumradius >1.58 mm, average radius >0.86 mm, and inradius >0.35 mm) and small radii (circumradius <0.48 mm, average radius <0.37 mm, and inradius <0.17 mm) account for a small proportion of all the patches, whereas the proportion of patches with medium radii predominates.

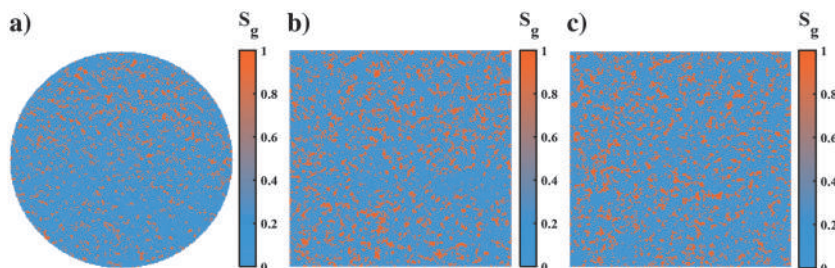


Figure 4. The gas-saturation map of the (a) XY, (b) XZ, and (c) YZ sections. Here, S_g indicates gas saturation.

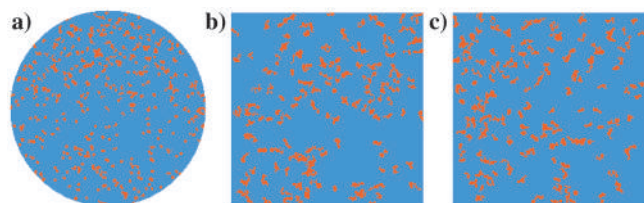


Figure 5. A binary map of the (a) XY, (b) XZ, and (c) YZ sections.

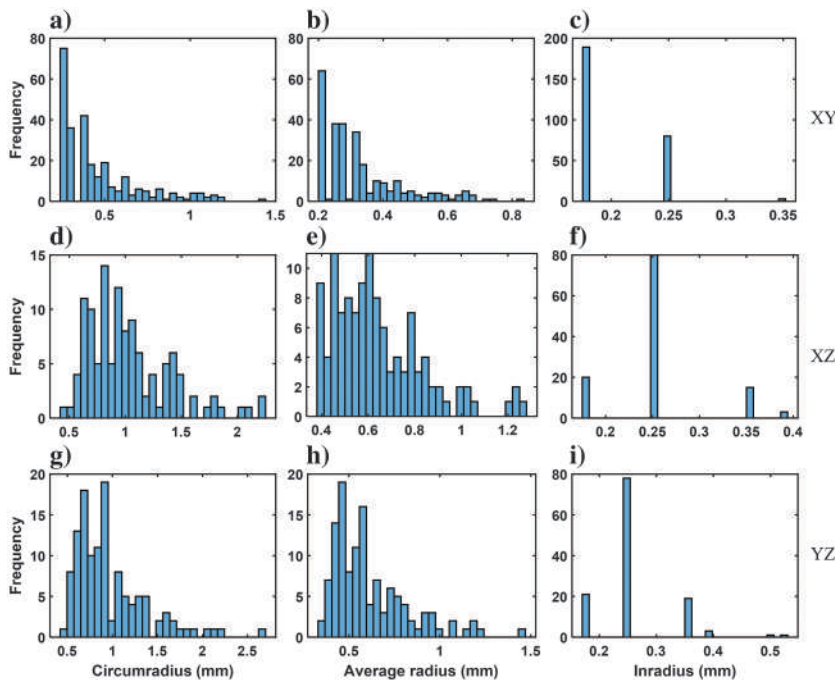


Figure 6. Statistical frequency distribution histograms of the different radii in different sections: (a, d, and g) circumradius, (b, e, and h) average radius, and (c, f, and i) inradius.

Figure 7 shows the relationship between the radius and the volume fraction of the different sections. Each scatter point represents a gas patch of a particular size. More data scatters for smaller gas patch radii indicate that there are more small-sized gas patches within the sample. It is relevant to the pore structure and the fundamental physical properties of the core and fluids, where more small-sized gas pockets could be expected within the host fluid of water (e.g., see the results of Sun et al., 2023b). There is an apparent correlation, indicating that small-radius gas patches correspond to smaller volume fractions and occupy a smaller percentage of the pore space. As the radius increases, the corresponding volume fraction also increases and occupies more pore space. The calculated sum of all gas patch volume fractions in the three sections is as follows: 11.11% (XY), 10.98% (XZ), and 11.14% (YZ). These values are in good agreement with the gas saturation (11%).

THEORY

Based on the gas patch distribution shown in Figure 5, it is evident that each section contains hundreds of groups of gas patches with varying shapes. In the theoretical model of partially saturated rocks, the White model assumes a uniform size distribution of gas patches, whereas the continuous random media (CRM) model introduces an autocorrelation function to characterize the spatial distribution of gas patches within a certain size range. However, these models fail to account for the impact of gas patches at each distinct scale (e.g., those extracted from the CT images) on seismic wave propagation. The IPMPS model has the ability to address this limitation by assuming that there are two immiscible fluids with different properties, one relatively less compressible (e.g., water) and one highly compressible (e.g., gas). The former occupies a completely continuous volume of rock (the host) surrounding a dilute concentration of spherical gas-saturated patches (the inclusions). The inclusions are divided into infinite groups of additions with the same properties, such as density, viscosity, and volume fraction, and different sizes. These patches are gradually introduced into the host phase of a fully water-saturated rock to achieve a partial-saturation state. Figure 8 shows a diagram of adding inclusions of different sizes. The specific equation of the IPMPS model is provided in Appendix A.

The order of the addition of the patches

To investigate the influence of the order in which the inclusions are added, the XZ section serves as an example. We inserted the statistically determined radius and volume fractions from Figure 7d to 7f into the model in two different ways: first, by adding them sequentially from the smallest to the largest inclusion, and second, by adding them in random order. Further properties are shown in Table 1. The results are shown in Figure 9. It was found that the order in which patches are added has a minimal effect on the result. Therefore, in the following, the gas patches are added in order from the smallest to the largest patch.

Sensitivity analysis

To validate the robustness of the IPMPS model, we applied the Sobol method to perform a sensitivity analysis for the parameters provided in Table 1. The Sobol method, a variance-based Monte Carlo technique, serves as a form of global sensitivity analysis. In this method, the model is decomposed into functions that include individual input parameters and combinations of multiple input parameters. By evaluating the impact of the variance of individual or multiple input parameters on the total variance of the output, the Sobol sensitivity indices are calculated. These indices are defined as follows (Sobol, 2001):

$$S_{i_1 \dots i_s} = \frac{D_{i_1 \dots i_s}}{D}, \quad (7)$$

where D is the variance and $D_{i_1 \dots i_s}$ denotes the partial variance corresponding to the subset of parameters. For the i th input parameter, $S_i = (D_i/D)$ represents the first-order sensitivity index, $S_{ij} = (D_{ij}/D)$ denotes the second-order sensitivity index, and $S_{T_i} = S_i + S_{ij} + \dots + S_{1 \dots i \dots s}$ represents the total-order sensitivity index. In general, the first-order sensitivity indices and the total-order sensitivity index are used to measure the importance of the input parameters: the first-order sensitivity index serves as an indicator that measures the contribution of a single parameter to the variance of the output. A larger first-order sensitivity index indicates a greater influence of this parameter on the variance of the output. In contrast, the total-order sensitivity index evaluates the contribution of an individual parameter and its interaction with other parameters to the output variance. The difference between the total- and first-order sensitivity indices reflects the size of the contribution of the interaction between the parameter and other parameters to the variance of the output.

We have selected four key properties for the analysis: porosity, permeability, water, and gas viscosity. The variation range of these properties is shown in Table 2. Their effects on the bulk modulus and attenuation were investigated at frequencies of 40 and 400 Hz. Figure 10a and 10b shows the influence of these properties on the bulk modulus and attenuation at a frequency of 40 Hz. It can be seen that permeability and water viscosity individually have the greatest influence on the bulk modulus, whereas the interaction between the

properties has a smaller effect. Porosity, permeability, and water viscosity have a certain influence on the attenuation when considered individually, whereas permeability and water viscosity have a stronger influence on the attenuation when they interact with other properties. Figure 10c and 10d shows the effects of the properties on the bulk modulus and attenuation at a frequency of 400 Hz. Porosity and water viscosity have a greater influence on the bulk modulus when considered separately. Similarly, porosity, permeability, and water viscosity all have a significant effect on attenuation when

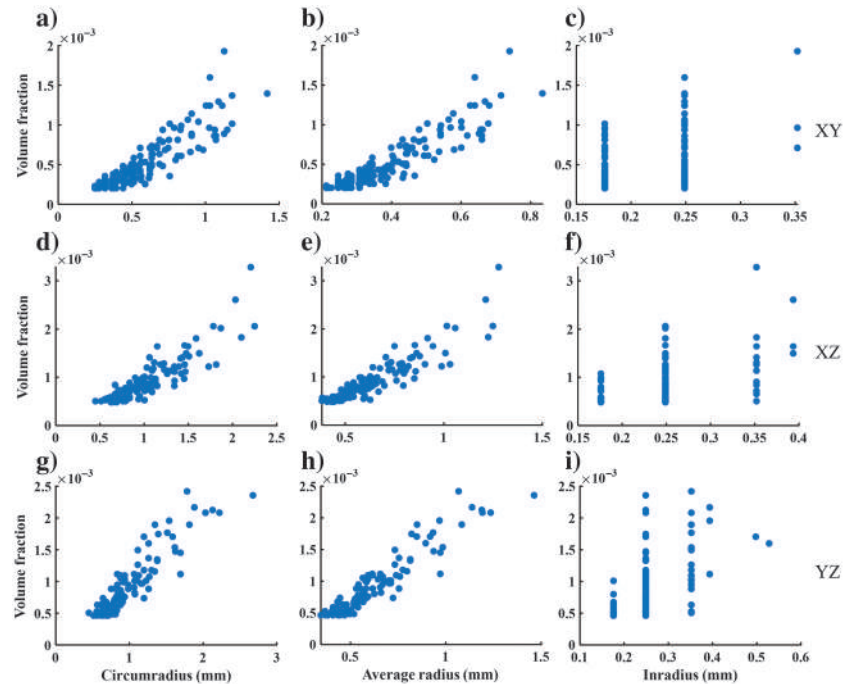


Figure 7. The relationship between the different gas patch radii (r) and the volume fraction (v) of the different sections: (a, d, and g) circumradius, (b, e, and h) average radius, and (c, f, and i) inradius.

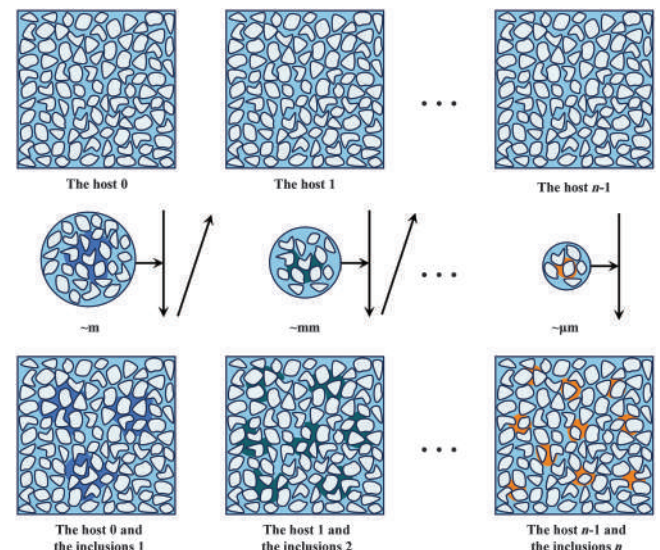


Figure 8. Schematic diagram of adding inclusions.

considered individually. Although there is some influence, the interaction between the properties has a minimal effect on the bulk modulus and attenuation. The influence of gas viscosity on the model prediction results is negligible and can be ignored.

RESULTS

Example with statistical data

Based on the statistical analysis, the gas patch radii (r) and volume fraction (v) in Figure 7 are considered as inputs to equations A-1–A-4.

Table 2. Ranges in the sensitivity analysis.

	Lower limit	Upper limit
Porosity (%) ϕ	5	15
Permeability (m^2) κ	2×10^{-18}	2×10^{-16}
Water viscosity (Pa·s) η_f^H	10^{-4}	10^{-2}
Air viscosity (Pa·s) η_f^I	2×10^{-6}	2×10^{-4}

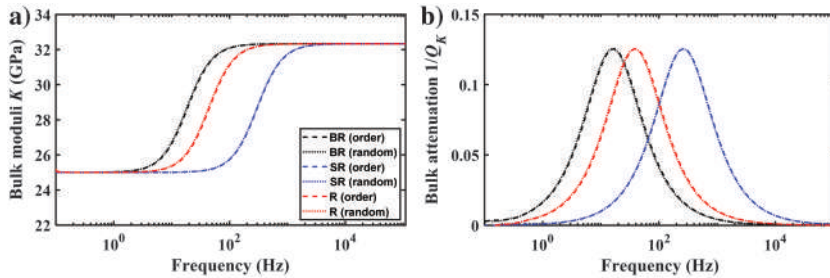


Figure 9. The effect of the different additions of gas patches in the XZ section on the model predictions for (a) bulk modulus and (b) attenuation. The dotted lines are added in order from small to large and the dotted lines are added in random order.

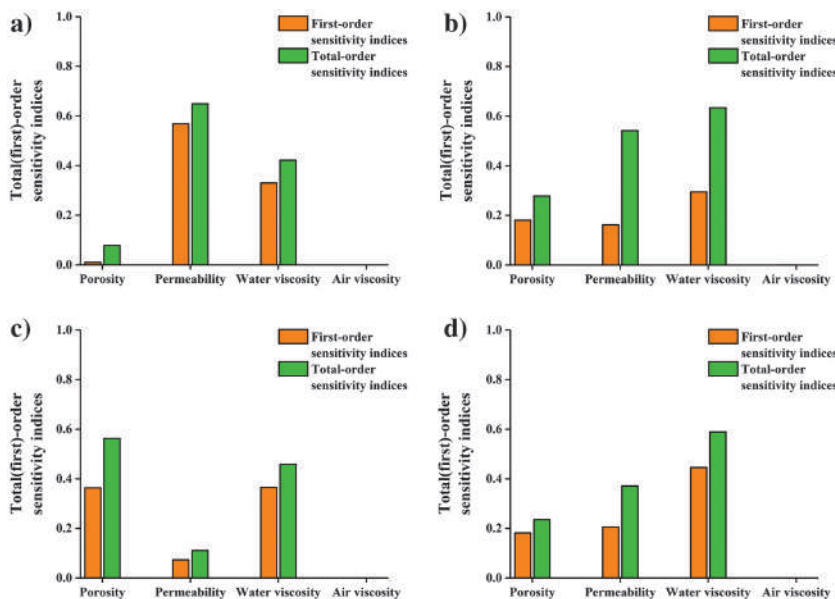


Figure 10. The effect of porosity, permeability, water viscosity, and air viscosity on the model predictions. (a and b) The predicted bulk modulus and attenuation of 40 Hz, respectively, and (c and d) the predicted bulk modulus and attenuation of 400 Hz, respectively.

The results from equations A-18 to A-20 are compared with experimental data for a rock with 89% water saturation during the drainage process. The properties are shown in Table 1.

Figure 11 compares the theoretical and experimental bulk modulus (K) and attenuation (dissipation factor, $1/Q_K$) for the different sections at 89% water saturation. In Figure 11a, $R^2 = 0.8217$ (BR), $R^2 = 0.6669$ (R), and $R^2 = 0.3840$ (SR) (the bulk modulus). In Figure 11b, $R^2 = 0.6749$ (BR), $R^2 = 0.6198$ (R), and $R^2 = 0.5839$ (SR) (attenuation). In Figure 11c, $R^2 = 0.9442$ (BR), $R^2 = 0.9484$ (R), and $R^2 = 0.4228$ (SR) (the bulk modulus). In Figure 11d, $R^2 = 0.8864$ (BR), $R^2 = 0.8300$ (R), and $R^2 = 0.5845$ (SR) (attenuation). In Figure 11e, $R^2 = 0.9488$ (BR), $R^2 = 0.9430$ (R), and $R^2 = 0.4329$ (SR) (the bulk modulus). In Figure 11f, $R^2 = 0.9021$ (BR), $R^2 = 0.8091$ (R), and $R^2 = 0.5870$ (SR) (attenuation). The results for sections XZ and YZ are in better agreement with the experimental data than those for section XY. Due to the strong heterogeneity of the pore structure, the pore shapes are different in different directions, and there is a density difference between gas and water, resulting in differences in the fluid distribution in different directions. The XZ and YZ sections can better represent the main shapes of fluids in 3D rocks. Among the three sets of radii and volume fractions, those of the average radius (the red curves) agree better with the data. In the following discussions, the average radius is considered the representative radius for gas patches.

The results for the bulk modulus are generally consistent with the data. However, at low frequencies (<1 Hz), the predicted bulk modulus is slightly higher. The dry-rock bulk modulus (K_b) was measured at the confining pressure of 5 MPa. Compared with zero confining pressure, a few cracks have closed, resulting in a predicted bulk modulus higher than the experimental one. Attenuation follows a similar frequency-dependent trend as the experimental data. The theoretical peak attenuation is higher than the experimental one, which could be due to subtle differences between the fluid distributions obtained from the 2D sections and the real conditions.

Example with fractal dimension

Previous work states that fluid distribution has fractal characteristics (Feder, 1988; Müller et al., 2008; Zhang et al., 2015). We classify the gas patches in the binary map of Figure 5 by the box counting method (Liebovitch and Toth, 1989). The fractal dimensions D_f of the three sections are: the XY section: 1.4826, the XZ section: 1.3907, and the YZ section: 1.4507. Based on the relationship between porosity and the measurement scale proposed by Rieu and Perrier (1998), the volume fraction of the embedded inclusion as a function of the inclusion sizes is

$$v_l = 1 - (r_{\min}/r_{\max})^{D_E - D_f}, \quad (8)$$

where D_E is the Euclidean dimension, D_f is the fractal dimension, and r_{\min} and r_{\max} are the minimum and maximum inclusion radii, respectively.

These quantities for the gas patches are obtained by the statistical analysis of the three sections and then substituted into equation 8 to estimate the corresponding volume fractions. The inclusion is divided into 25 parts and added to the IPMPS model. In fact, the IPMPS model theoretically allows for the division of the inclusions into infinite (much more than 25) parts. To reduce the computational cost and maintain the accuracy of the predictions, it is found that dividing the inclusions into 25 parts yields acceptable simulation results. The radius and volume fraction satisfy the fractal (self-similar) distribution. The properties are provided in Table 1.

Figure 12 compares the modeling results obtained using the average radius (in red) and fractal dimension (in blue) with the experimental data (in circles). In Figure 12a, $R^2 = 0.6669$ (R) and $R^2 = 0.7668$ (D_f) (the bulk modulus). In Figure 12b, $R^2 = 0.6198$ (R) and $R^2 = 0.6414$ (D_f) (attenuation). In Figure 12c, $R^2 = 0.9484$ (R) and $R^2 = 0.9515$ (D_f) (the bulk modulus). In Figure 12d, $R^2 = 0.8300$ (R) and $R^2 = 0.8480$ (D_f) (attenuation). In Figure 12e, $R^2 = 0.9430$ (R) and $R^2 = 0.9500$ (D_f) (the bulk modulus). In Figure 12f, $R^2 = 0.8091$ (R) and $R^2 = 0.8471$ (D_f) (attenuation). The results are in good agreement with the data, and those of the XZ and YZ sections show a better consistency. The velocity dispersion and attenuation can be used to directly estimate the gas patch radii and volume fractions or the fractal dimension by assuming a self-similar distribution.

Comparison with the CRM model

In the CRM model, correlation length is a key parameter for predicting wave velocities and attenuation (Toms et al., 2006, 2007). Toms-Stewart et al. (2009) propose a method to determine the Debye length as a substitute for the correlation length, and the

correlation function in a binary map can be derived based on the probability of random points falling into two distinct regions:

$$\chi(l) = S_w(l, l + dl) - S_w(l)^2, \quad (9)$$

where l is the correlation lag and $S_w(l, l + dl)$ is the two-point probability function for the water-saturated domain, where this function refers to the probability that two random points displaced by a scalar distance dl are located in that domain. The function is determined using the Monte Carlo method (Hammersley, 2013). In addition, $S_w(l)$ is the single-point probability function for the water-saturated domain, i.e., it is based on randomly generating a point on the binary map and recording the number of times for which it falls within the water-saturated area divided by the number of all random points. It is equivalent to the volume fraction of the water-saturated region in the binary map.

Figure 13 illustrates the correlation functions of different sections as a function of the correlation lag, showing an exponentially decreasing trend. Toms-Stewart et al. (2009) consider that the correlation functions change with fluid saturation and rock type. This study shows that the differences in the correlation functions for the 2D sections can be related to the distinct flow patterns in different directions.

By assuming a binary map representing a Debye random material, the Debye correlation length can be obtained using the correlation function (Debye and Bueche, 1949)

$$\chi(l) = \exp\left(\frac{-|l|}{a}\right), \quad (10)$$

where a is the Debye correlation length. The Debye correlation lengths of the three sections XY, XZ, and YZ are 0.332, 0.433, and 0.432 mm, respectively, obtained by substituting a into the

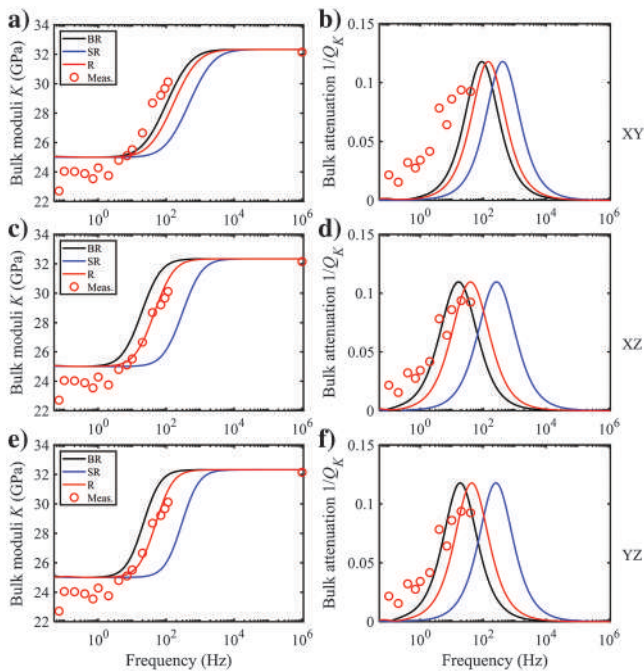


Figure 11. A comparison between the theory and the experiment for the (a and b) XY, (c and d) XZ, and (e and f) YZ sections. Here, BR, SR, and R indicate the results corresponding to the circumradius, inradius, and average radius, respectively. The red circles are the measured data.

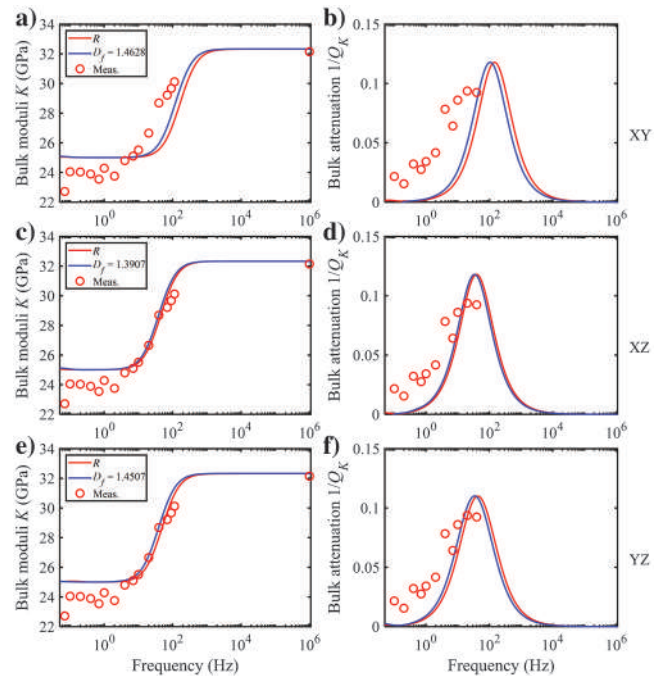


Figure 12. A comparison between the theory and the experiment for the (a and b) XY, (c and d) XZ, and (e and f) YZ sections obtained with the average radius (in red) and the fractal dimension (in blue). The red circles are the measured data.

CRM model. Except for the correlation length, the other modeling parameters are the same as those of the IPMPS model.

Figure 14 shows the effects of correlation length on the CRM model. In Figure 14a, $R^2 = 0.6669$ (XY), $R^2 = 0.9484$ (XZ), and $R^2 = 0.9430$ (YZ) (the bulk modulus by the IPMPS model), and $R^2 = 0.3879$ (XY), $R^2 = 0.4446$ (XZ), and $R^2 = 0.4442$ (YZ) (the bulk modulus by the CRM model). In Figure 14b, $R^2 = 0.6198$ (XY), $R^2 = 0.8300$ (XZ), and $R^2 = 0.8091$ (YZ) (attenuation by the IPMPS model) and $R^2 = 0.6568$ (XY), $R^2 = 0.6850$ (XZ), and $R^2 = 0.6848$ (YZ) (attenuation by the CRM model). As the length increases, the dispersion and the attenuation shift toward lower frequencies. In contrast to the IPMPS model, the

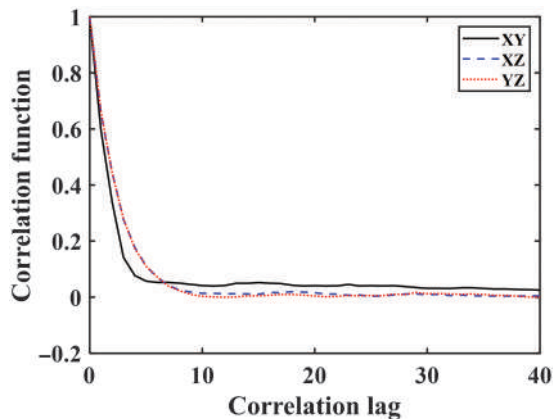


Figure 13. Correlation functions for the different sections. The lag is the number of pixels.

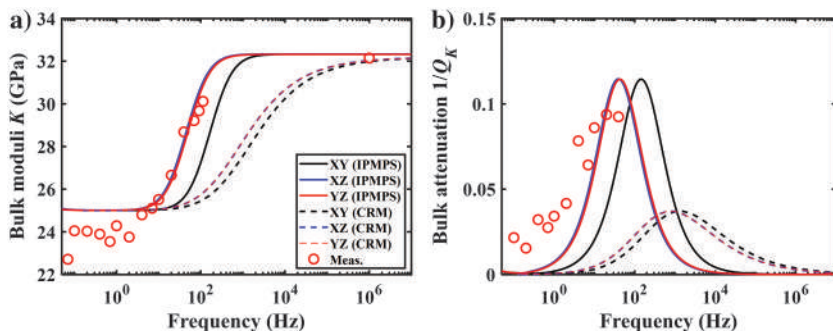


Figure 14. A comparison between the IPMPS and CRM models for (a) bulk modulus and (b) attenuation. The red circles are the measured data.

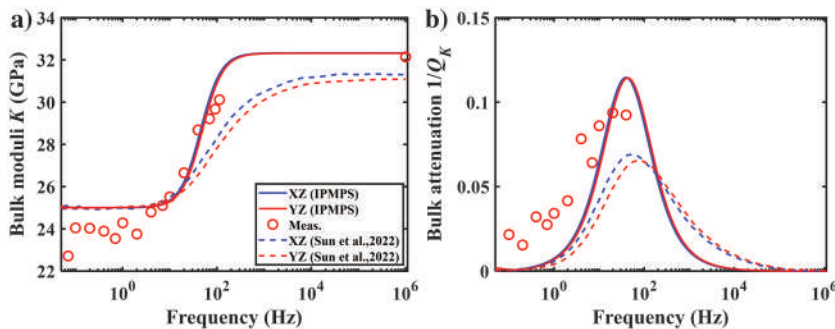


Figure 15. (a and b) A comparison between the IPMPS model and the finite-element-based model for (a) bulk modulus and (b) attenuation. The red circles are the measured data.

CRM model results show little difference between the sections. Figure 14a shows that the two models have the same bulk moduli at the low- and high-frequency limits. The IPMPS model shows a narrower band of anelasticity ($2.7\text{--}8.3 \times 10^2$ Hz) and agrees well with the experimental data, whereas the CRM model shows a wider dispersion band ($5.6\text{--}1.6 \times 10^6$ Hz). This discrepancy could be due to the fact that the Debye correlation length is an approximation and cannot fully reproduce the scales of the gas patches in the binary map. In Figure 14b, it can be seen that the CRM model predicts significantly lower attenuation compared with the IPMPS model. In addition, the characteristic frequency of the peak attenuation of the IPMPS model is lower and agrees better with the experimental data, whereas the CRM model predicts a higher characteristic frequency.

Figure 7 shows that the proportion of gas patches with a small radius is also very small. The correlation lengths in the CRM model of the three sections are close to the statistical minimum radius limit. They can only reflect the size of a very small part of the gas patches and cannot be used to represent all gas patches. As a result, the predictions of the CRM model are suboptimal. The biggest advantage of the IPMPS model is that it can replace gas spots of different sizes one after another, which makes it an effective tool for studying multiscale fluid distribution.

Comparison with the finite-element method

Figure 15 shows the comparison between the IPMPS model and that of Sun et al. (2022) based on finite elements. In Figure 15a, $R^2 = 0.9484$ (XZ) and $R^2 = 0.9430$ (YZ) (the bulk modulus by the IPMPS model), and $R^2 = 0.9080$ (XZ) and $R^2 = 0.8725$ (YZ) (the bulk modulus by Sun et al., 2022). In Figure 15b, $R^2 = 0.8300$ (XZ) and $R^2 = 0.8091$ (YZ) (attenuation by the IPMPS model), and $R^2 = 0.8673$ (XZ) and $R^2 = 0.8255$ (YZ) (attenuation by Sun et al., 2022). At low frequencies (<18 Hz), the predictions of the two methods are consistent. However, as the frequency increases, the IPMPS model predicts higher moduli and attenuation. Figure 15a shows that the moduli determined by the IPMPS model agree better with the data. Figure 15b shows that both methods predict the characteristic frequency of peak attenuation. At low frequencies (<20 Hz), the attenuations of both models are lower than the experimental values. In the frequency range around the peak (>20 Hz), the IPMPS model predicts higher attenuation. The finite-element method allows for precise simulations of structural, thermal, and fluid dynamics behaviors by discretizing the domain into smaller and manageable elements. This approach is particularly useful for predicting responses in heterogeneous materials and systems under various loading conditions, making it a valuable tool for research and practical engineering applications. The IPMPS model fully considers the impact of gas patch size on seismic wave dispersion and can predict variations in the seismic wave velocity for different saturations. The method is well suited for applications involving heterogeneous rocks caused by differences in fluid properties.

A comparison of prediction results for different sections in the same direction

We have considered the three different sections in the XY direction: XY1 (the same as the XY section mentioned in Figure 3a), XY2, and XY3, whose spatial locations are shown in Figure 16a. By using the same processing steps as described, we obtain the gas-saturation maps with the corresponding binary images shown in Figure 16b–16d. The number of gas patches in the XY3 section is obviously lower than those in the XY1 and XY2 sections. The calculations show that the total volume fractions of the pockets in the binary images are as follows: 11.11% (XY1), 12.11% (XY2), and 7.04% (XY3). Figure 16 shows that the gas-water distribution in different sections in the XY direction is influenced by gravity, with more gas distributed in the upper layers of the core sample and more water concentrated in the lower layers. Figure 17 shows a comparison of the model predictions for different sections. The predictions for XY1 and XY2 are similar, whereas the difference in gas saturation between the sections leads to deviations in the

prediction for XY3. The bulk modulus is higher overall, with slightly larger attenuation and a shift to lower frequencies.

From the results in Figures 16 and 17, it is evident that, due to the influence of gravity, there are significant differences in fluid saturation between 2D sections in the XY direction, making it difficult to select an appropriate 2D section to represent the entire 3D rock. Therefore, the 2D sections in the XY direction are not representative of the whole sample. By comparing the prediction results in all three directions, it is observed that in the XZ and YZ directions, the fluid saturation obtained from the 2D sections is similar to that of the entire rock, and the predicted results match well with the measured bulk modulus and attenuation, whereas the prediction results from the XY section differ more significantly. This suggests that the sections in the XZ and YZ directions are less influenced by gravity and can better represent the overall rock.

CONCLUSION

We use CT scan images to obtain information on fluid distribution in partially saturated rocks and perform statistical analysis of the gas patches. This information is used to calculate the wave attenuation and velocity dispersion caused by the local fluid flow at the mesoscopic scale using the IPM with partial saturation. The results show a good agreement with the experimental data. It has been shown that the use of CT scan information to replace the assumed fluid distribution scenarios in the model is feasible. Application of the workflow presented here to other samples also could be considered in future work.

We use other methods to calculate the wave anelasticity, namely, one based on the fractal dimension and another based on the finite-element method. Comparisons show that the present model provides better agreement with the experimental data, although the difference between the predictions of the model based on directly measured fluid distributions and those based on the estimated fractal dimension is small. In the XY direction, comparisons among the different sections indicate that the effect of gravity plays a role in the gas-water distribution in the rock sample. By extracting the gas patches' radii and volume fractions from the CT scan images of the rock samples and inputting them into the IPMPS model for prediction, the theoretical results have achieved an R^2 value of up to 0.94 compared with the experimental data. The method is applicable to effectively predict the seismic wave dispersion and attenuation responses, providing a quantitative link between seismic attributes and pore fluid distribution.

In this work, the radii and volume fractions of the three used sections may be close to the averaged ones, although there are some mismatches of the modulus dispersion and $1/Q$ in the low-frequency range. In the rock-physics studies probing into the detailed microstructures of rock samples, each sample could be different, and one can never have two identical rock samples, leading to endless challenges. The work presented here can be one of the showcases if we need to dig into the microscale structures of rocks, whereas seismic data cannot have such a high resolution.

ACKNOWLEDGMENTS

We appreciate the financial support from the National Natural Science Foundation of China (no. 42174161). We thank the journal editors

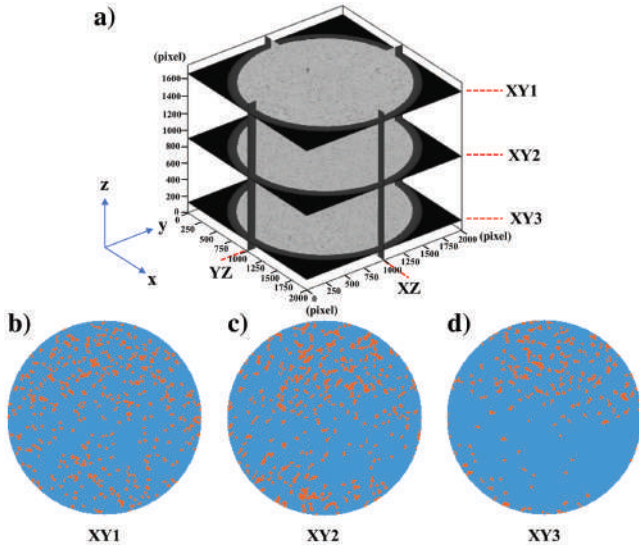


Figure 16. Spatial locations of the three sections in the XY direction and their corresponding binary images. (a) Spatial locations of the three sections (XY1, XY2, and XY3) and (b–d) the binary images corresponding to these sections.

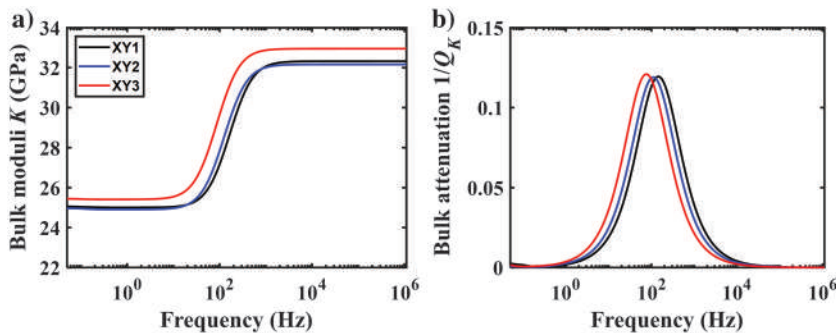


Figure 17. Model predictions for the different sections in the XY direction for (a) bulk modulus and (b) attenuation.

(A. Guitton, A. Malcolm, S. Hestholm, and K. Innanen) and the reviewers for their constructive feedback.

DATA AND MATERIALS AVAILABILITY

Data associated with this research are available and can be obtained by contacting the corresponding author.

APPENDIX A

IPM WITH PARTIAL SATURATION

The corresponding equations for wave propagation are (Zhang et al., 2022)

$$\begin{aligned}
 & (N + NZ\phi_0 dS)\nabla^2 \mathbf{u} + (A + N)\nabla e + (A_d + NZ)\phi_0 dS \nabla e \\
 & + Q_H \phi_0 S \nabla (\xi_H + \zeta \phi_0 dS) \\
 & + R_H \left(\frac{Q_1}{K_f^I} - \frac{Q_1}{K_s} - 1 \right) \phi_0 dS \nabla \xi_H + Q_1 \phi_0 dS \nabla (\xi_I - \phi_0 S \zeta) \\
 & = \rho_{00} \ddot{\mathbf{u}} + (\rho_{00} Z - \rho_s - \rho_{02}) \phi_0 dS \ddot{\mathbf{u}} + \rho_{01} \phi_0 S \ddot{\mathbf{U}}_H \\
 & + \rho_{01} \phi_0^2 Z dS \ddot{\mathbf{U}}_H + \rho_{02} \phi_0 dS \ddot{\mathbf{U}}_I + \frac{\phi_0^2 S \eta_f^H}{\kappa_H} (\dot{\mathbf{u}} - \dot{\mathbf{U}}_H) \\
 & + \frac{\phi_0^3 S \eta_f^H}{\kappa_H} Z dS (\dot{\mathbf{u}} - \dot{\mathbf{U}}_H) + \frac{\phi_0^2 \eta_f^I dS}{\kappa_I} (\dot{\mathbf{u}} - \dot{\mathbf{U}}_I), \quad (\text{A-1})
 \end{aligned}$$

$$\begin{aligned}
 & Q_H \nabla e + R_H \nabla (\xi_H + \zeta \phi_0 dS) + \frac{R_H}{\phi} (\nabla \xi_H - \nabla e) \phi_0 dS \\
 & = \left(1 + \frac{R_H}{S} \left(\frac{1}{K_f^H} - \frac{1}{K_s} \right) dS \right) \left(\rho_{01} \ddot{\mathbf{u}} + \rho_{11} \ddot{\mathbf{U}}_H - \frac{\phi_0 \eta_f^H}{\kappa_H} (\dot{\mathbf{u}} - \dot{\mathbf{U}}_H) \right), \quad (\text{A-2})
 \end{aligned}$$

$$Q_1 \nabla e + R_1 \nabla (\xi_I - \phi_0 S \zeta) = \rho_{02} \ddot{\mathbf{u}} + \rho_{22} \ddot{\mathbf{U}}_I - \frac{\phi_0 \eta_f^H}{\kappa_H} (\dot{\mathbf{u}} - \dot{\mathbf{U}}_I), \quad (\text{A-3})$$

$$\begin{aligned}
 & (Q_H e + R_H (\xi_H + \zeta \phi_0 dS)) - (Q_1 e + R_1 (\xi_I - \phi_0 S \zeta)) \\
 & = \frac{1}{3} r^2 \phi_0^2 S \left(\frac{\rho_f^H}{\phi_0} \ddot{\zeta} + \frac{\eta_f^H}{\kappa_H} \dot{\zeta} \right), \quad (\text{A-4})
 \end{aligned}$$

where \mathbf{u} , \mathbf{U}_H , and \mathbf{U}_I are the solid displacement and the fluid displacements of the two-pore phases, respectively; the water saturations (S) are equal to the volume fractions (v) of the host; ϕ_0 is the porosity of the host; e is the solid divergence field; ξ_H and ξ_I are the fluid strains of the two-pore phases saturated by the host and inclusion fluids, respectively; ζ denotes the fluid strain increment between the two pore phases; K_s , K_f^H , and K_f^I are the grain, host, and inclusion fluid bulk moduli, respectively; ρ_s and ρ_f^H are the densities of the grain and host fluid, respectively; κ_H and κ_I are the permeabilities of the host skeleton and inclusions, respectively; η_f^H and η_f^I are the viscosities of the host and inclusion fluids, respectively; and r is the inclusion radius. The stiffnesses A , A_d , N , Q_H , Q_1 , R_H , R_1 , and Z and the density coefficients ρ_{00} , ρ_{01} , ρ_{02} , ρ_{11} , and ρ_{22} are

$$A = (1 - \phi_0 S) K_s - \frac{2}{3} N - K_s / K_f^H Q_H \phi_0 S, \quad (\text{A-5})$$

$$\begin{aligned}
 A_d &= (1 - \phi_0 S) K_s Z - \frac{2}{3} N Z - Q_1 R_H (K_s / (K_f^H K_f^I) - 1 / K_f^I) \\
 &- Q_1 K_s / K_f^I + R_H K_s / K_f^H - K_s, \quad (\text{A-6})
 \end{aligned}$$

$$N = G_b, \quad (\text{A-7})$$

$$Q_H = \frac{K_s (1 - \phi_0 S - K_b / K_s)}{1 - \phi_0 S - K_b / K_s + K_s / K_f^H \phi_0 S}, \quad (\text{A-8})$$

$$Q_1 = \frac{K_s (1 - \phi_0 S - K_b / K_s)}{1 - \phi_0 S - K_b / K_s + K_s / K_f^I \phi_0 S}, \quad (\text{A-9})$$

$$R_H = \frac{K_s \phi_0 S}{1 - \phi_0 S - K_b / K_s + K_s / K_f^H \phi_0 S}, \quad (\text{A-10})$$

$$R_1 = \frac{K_s \phi_0 S}{1 - \phi_0 S - K_b / K_s + K_s / K_f^I \phi_0 S}, \quad (\text{A-11})$$

$$Z = R_H / (\phi_0 S) (1 / K_f^H - 1 / K_s) + R_1 / (\phi_0 S) (1 / K_f^I - 1 / K_s), \quad (\text{A-12})$$

$$\rho_{00} = (1 - \phi_0 S) \rho_s - \phi_0 \rho_{01}, \quad (\text{A-13})$$

$$\rho_{01} = (1 - \alpha) \rho_f^H, \quad (\text{A-14})$$

$$\rho_{02} = (1 - \alpha) \rho_f^I, \quad (\text{A-15})$$

$$\rho_{11} = \alpha \rho_f^H, \quad (\text{A-16})$$

$$\rho_{22} = \alpha \rho_f^I, \quad (\text{A-17})$$

where K_b and G_b are the dry-rock bulk and shear moduli, respectively; α is the tortuosity; and ρ_f^I is the density of the inclusion fluid.

The complex P and S wavenumbers (k_p and k_s) are obtained by a plane-wave analysis of equations A-1–A-4. In each iteration, equations B-1–B-4 of Ba et al. (2011) are solved (Zhang et al., 2022) to obtain the complex bulk and shear moduli of the composite porous medium:

$$K_{\text{sat}} = ((1 - \phi_0(S + dS))\rho_s + (S + dS)\rho_f) \left(\frac{\omega}{k_p} \right)^2 - \frac{4}{3} G_{\text{sat}}, \quad (\text{A-18})$$

$$G_{\text{sat}} = ((1 - \phi_0(S + dS))\rho_s + \phi_0(S + dS)\rho_f) \left(\frac{\omega}{k_s} \right)^2, \quad (\text{A-19})$$

where ω is the angular frequency and $\rho_f = \rho_f^H S_H + \rho_f^L S_L$ is the effective fluid density.

After the last iteration, when all the patches have been included, we obtain the final complex bulk modulus, and the dissipation factor is

$$Q_K^{-1} = \frac{\text{Im}(K_{\text{sat}})}{\text{Re}(K_{\text{sat}})}. \quad (\text{A-20})$$

REFERENCES

- Ba, J., J. M. Carcione, and J. X. Nie, 2011, Biot-Rayleigh theory of wave propagation in double-porosity media: *Journal of Geophysical Research: Solid Earth*, **116**, B06202, doi: [10.1029/2010JB008185](https://doi.org/10.1029/2010JB008185).
- Ba, J., R. Ma, J. M. Carcione, and S. Picotti, 2019, Ultrasonic wave attenuation dependence on saturation in tight oil siltstones: *Journal of Petroleum Science and Engineering*, **179**, 1114–1122, doi: [10.1016/j.petrol.2019.04.099](https://doi.org/10.1016/j.petrol.2019.04.099).
- Ba, J., J. X. Nie, H. Cao, and H. Z. Yang, 2008, Mesoscopic fluid flow simulation in double-porosity rocks: *Geophysical Research Letters*, **35**, L04303, doi: [10.1029/2007GL032429](https://doi.org/10.1029/2007GL032429).
- Ba, J., W. Xu, L. Y. Fu, J. M. Carcione, and L. Zhang, 2017, Rock anelasticity due to patchy saturation and fabric heterogeneity: A double double-porosity model of wave propagation: *Journal of Geophysical Research: Solid Earth*, **122**, 1949–1976, doi: [10.1002/2016JB013882](https://doi.org/10.1002/2016JB013882).
- Ba, J., X. F. Yan, Z. Y. Chen, G. C. Xu, C. S. Bian, H. Cao, F. C. Yao, and W. T. Sun, 2013, Rock physics model and gas saturation inversion for heterogeneous gas reservoirs: *Chinese Journal of Geophysics*, **56**, 1696–1706, doi: [10.6038/cjg20130527](https://doi.org/10.6038/cjg20130527).
- Ba, J., L. Zhang, W. Sun, and Z. Hao, 2014, Velocity field of wave-induced local fluid flow in double-porosity media: *Science China Physics, Mechanics & Astronomy*, **57**, 1020–1030, doi: [10.1007/s11433-014-5442-0](https://doi.org/10.1007/s11433-014-5442-0).
- Bear, J., 1972, *Dynamics of fluids in porous media*: Elsevier.
- Borgomano, J. V., L. X. Pimenta, J. Fortin, and Y. Guéguen, 2019, Seismic dispersion and attenuation in fluid-saturated carbonate rocks: Effect of microstructure and pressure: *Journal of Geophysical Research: Solid Earth*, **124**, 12498–12522, doi: [10.1029/2019JB018434](https://doi.org/10.1029/2019JB018434).
- Cadoret, T., D. Marion, and B. Zinszner, 1995, Influence of frequency and fluid distribution on elastic wave velocities in partially saturated limestones: *Journal of Geophysical Research: Solid Earth*, **100**, 9789–9803, doi: [10.1029/95JB00757](https://doi.org/10.1029/95JB00757).
- Carcione, J. M., H. B. Helle, and N. H. Pham, 2003, White's model for wave propagation in partially saturated rocks: Comparison with poroelastic numerical experiments: *Geophysics*, **68**, 1389–1398, doi: [10.1190/1.1598132](https://doi.org/10.1190/1.1598132).
- Carcione, J. M., and S. Picotti, 2006, P-wave seismic attenuation by slow-wave diffusion: Effects of inhomogeneous rock properties: *Geophysics*, **71**, no. 3, O1–O8, doi: [10.1190/1.2194512](https://doi.org/10.1190/1.2194512).
- Chapman, S., J. V. Borgomano, B. Quintal, S. M. Benson, and J. Fortin, 2021, Seismic wave attenuation and dispersion due to partial fluid saturation: Direct measurements and numerical simulations based on X-ray CT: *Journal of Geophysical Research: Solid Earth*, **126**, e2021JB021643, doi: [10.1029/2021JB021643](https://doi.org/10.1029/2021JB021643).
- Debye, P., and A. M. Bueche, 1949, Scattering by an inhomogeneous solid: *Journal of Applied Physics*, **20**, 518–525, doi: [10.1063/1.1698419](https://doi.org/10.1063/1.1698419).
- Deng, J. X., S. X. Wang, and W. Du, 2012, A study of the influence of mesoscopic pore fluid flow on the propagation properties of compressional wave — A case of periodic layered porous media: *Chinese Journal of Geophysics*, **55**, 2716–2727, doi: [10.6038/j.issn.0001-5733.2012.08.024](https://doi.org/10.6038/j.issn.0001-5733.2012.08.024).
- Dutta, N. C., and A. J. Seriff, 1979, On White's model of attenuation in rocks with partial gas saturation: *Geophysics*, **44**, 1806–1812, doi: [10.1190/1.1440940](https://doi.org/10.1190/1.1440940).
- Feder, J., 1988, *Fractals*: Plenum.
- Guo, J., and B. Gurevich, 2020, Frequency-dependent P wave anisotropy due to wave-induced fluid flow and elastic scattering in a fluid-saturated porous medium with aligned fractures: *Journal of Geophysical Research: Solid Earth*, **125**, e2020JB020320, doi: [10.1029/2020JB020320](https://doi.org/10.1029/2020JB020320).
- Hammersley, J., 2013, *Monte Carlo methods*: Springer Science & Business Media.
- Hart, D. J., and H. F. Wang, 1995, Laboratory measurements of a complete set of poroelastic moduli for Berea sandstone and Indiana limestone: *Journal of Geophysical Research: Solid Earth*, **100**, 17741–17751, doi: [10.1029/95JB01242](https://doi.org/10.1029/95JB01242).
- Ji, Y., P. Baud, V. Vajdova, and T. F. Wong, 2012, Characterization of pore geometry of Indiana limestone in relation to mechanical compaction: *Oil & Gas Science and Technology — Revue d'IFP Energies Nouvelles*, **67**, 753–775, doi: [10.2516/ogst/2012051](https://doi.org/10.2516/ogst/2012051).
- Johnson, D. L., 2001, Theory of frequency dependent acoustics in patchy-saturated porous media: *The Journal of the Acoustical Society of America*, **110**, 682–694, doi: [10.1121/1.1381021](https://doi.org/10.1121/1.1381021).
- Ketcham, R. A., and W. D. Carlson, 2001, Acquisition, optimization and interpretation of X-ray computed tomographic imagery: Applications to the geosciences: *Computers & Geosciences*, **27**, 381–400, doi: [10.1016/S0098-3004\(00\)00116-3](https://doi.org/10.1016/S0098-3004(00)00116-3).
- Kobayashi, Y., and G. Mavko, 2016, Variation in P-wave modulus with frequency and water saturation: Extension of dynamic-equivalent-medium approach: *Geophysics*, **81**, no. 5, D479–D494, doi: [10.1190/geo2015-0045.1](https://doi.org/10.1190/geo2015-0045.1).
- Kumar, M., J. Bhagwan, P. Kaswan, X. Liu, and M. Kumari, 2023, Inhomogeneous waves propagation in double-porosity thermoelastic media: *International Journal of Numerical Methods for Heat & Fluid Flow*, **33**, 2927–2962, doi: [10.1108/HFF-03-2023-0146](https://doi.org/10.1108/HFF-03-2023-0146).
- Kumar, M., M. Lal, N. Kumari, P. Kaswan, and M. Kumari, 2024, Inhomogeneous wave propagation in triple-porosity medium: *Journal of Vibration Engineering & Technologies*, **12**, 967–983, doi: [10.1007/s42417-024-01457-2](https://doi.org/10.1007/s42417-024-01457-2).
- Kumar, M., X. Liu, K. K. Kalkal, V. Dalal, and M. Kumari, 2022, Inhomogeneous wave reflection from the surface of a partially saturated thermoelastic porous media: *International Journal of Numerical Methods for Heat & Fluid Flow*, **32**, 1911–1943, doi: [10.1108/HFF-04-2021-0279](https://doi.org/10.1108/HFF-04-2021-0279).
- Liebowitch, L. S., and T. Toth, 1989, A fast algorithm to determine fractal dimensions by box counting: *Physics Letters A*, **141**, 386–390, doi: [10.1016/0375-9601\(89\)90854-2](https://doi.org/10.1016/0375-9601(89)90854-2).
- Liu, J., J. W. Ma, and H. Z. Yang, 2010, Research on P-wave's propagation in White's sphere model with patchy saturation: *Chinese Journal of Geophysics*, **53**, 954–962, doi: [10.3969/j.issn.0001-5733.2010.04.020](https://doi.org/10.3969/j.issn.0001-5733.2010.04.020).
- Michalopoulos, L. P., and G. E. Triandafyllidis, 1976, Influence of water on hardness, strength and compressibility of rock: *Environmental & Engineering Geoscience*, **13**, 1–22, doi: [10.2113/gsegeosci.xiii.1.1](https://doi.org/10.2113/gsegeosci.xiii.1.1).
- Müller, T. M., and B. Gurevich, 2004, One-dimensional random patchy saturation model for velocity and attenuation in porous rocks: *Geophysics*, **69**, 1166–1172, doi: [10.1190/1.1801934](https://doi.org/10.1190/1.1801934).
- Müller, T. M., B. Gurevich, and M. Lebedev, 2010, Seismic wave attenuation and dispersion resulting from wave-induced flow in porous rocks — A review: *Geophysics*, **75**, no. 5, A147–A164, doi: [10.1190/1.3463417](https://doi.org/10.1190/1.3463417).
- Müller, T. M., J. Toms-Stewart, and F. Wenzlau, 2008, Velocity-saturation relation for partially saturated rocks with fractal pore fluid distribution: *Geophysical Research Letters*, **35**, L09306, doi: [10.1029/2007GL033074](https://doi.org/10.1029/2007GL033074).
- Murphy, W. F., 1982, Effects of partial water saturation on attenuation in Massillon sandstone and Vycor porous glass: *The Journal of the Acoustical Society of America*, **71**, 1458–1468, doi: [10.1121/1.387843](https://doi.org/10.1121/1.387843).
- Pride, S. R., J. G. Beryman, and J. M. Harris, 2004, Seismic attenuation due to wave-induced flow: *Journal of Geophysical Research: Solid Earth*, **109**, B01201, doi: [10.1029/2003JB002639](https://doi.org/10.1029/2003JB002639).
- Qi, Q., T. M. Müller, B. Gurevich, S. Lopes, M. Lebedev, and E. Caspari, 2014, Quantifying the effect of capillarity on attenuation and dispersion in patchy-saturated rocks: *Geophysics*, **79**, no. 5, WB35–WB50, doi: [10.1190/geo2013-0425.1](https://doi.org/10.1190/geo2013-0425.1).
- Rieu, M., and E. Perrier, 1998, Fractal models of fragmented and aggregated soils, in B. Philippe, P. Jean-Yves, and A. S. Bobby, eds., *Fractals in soil science*: CRC Press, *Advances in Soil Science Series*, 169–202.
- Sharma, M. D., and M. Kumar, 2011, Reflection of attenuated waves at the surface of a porous solid saturated with two immiscible viscous fluids: *Geophysical Journal International*, **184**, 371–384, doi: [10.1111/j.1365-246X.2010.04841.x](https://doi.org/10.1111/j.1365-246X.2010.04841.x).
- Sobol, I. M., 2001, Global sensitivity indices for nonlinear mathematical models and their Monte Carlo estimates: *Mathematics and Computers in Simulation*, **55**, 271–280, doi: [10.1016/S0378-4754\(00\)00270-6](https://doi.org/10.1016/S0378-4754(00)00270-6).
- Solazzi, S. G., L. Guarracino, J. G. Rubino, and K. Holliger, 2019, Saturation hysteresis effects on the seismic signatures of partially saturated

- heterogeneous porous rocks: *Journal of Geophysical Research: Solid Earth*, **124**, 11316–11335, doi: [10.1029/2019JB017726](https://doi.org/10.1029/2019JB017726).
- Sun, C., J. Fortin, J. V. M. Borgomano, S. Wang, G. Tang, T. Bultreys, and V. Cnudde, 2022, Influence of fluid distribution on seismic dispersion and attenuation in partially saturated limestone: *Journal of Geophysical Research: Solid Earth*, **127**, e2021JB023867, doi: [10.1029/2021JB023867](https://doi.org/10.1029/2021JB023867).
- Sun, C., J. Fortin, G. Tang, and S. Wang, 2023a, Prediction of dispersion and attenuation on elastic wave velocities in partially saturated rock based on the fluid distribution obtained from three-dimensional (3D) micro-CT images: *Frontiers in Earth Science*, **11**, 1267522, doi: [10.3389/feart.2023.1267522](https://doi.org/10.3389/feart.2023.1267522).
- Sun, N., X. Yao, J. Liu, J. Li, N. Yang, G. Zhao, and C. Dai, 2023b, Breakup and coalescence mechanism of high-stability bubbles reinforced by dispersed particle gel particles in the pore-throat micromodel: *Geoenvironment Science and Engineering*, **223**, 211513, doi: [10.1016/j.geoen.2023.211513](https://doi.org/10.1016/j.geoen.2023.211513).
- Toms, J., T. M. Müller, R. Ciz, and B. Gurevich, 2006, Comparative review of theoretical models for elastic wave attenuation and dispersion in partially saturated rocks: *Soil Dynamics and Earthquake Engineering*, **26**, 548–565, doi: [10.1016/j.soildyn.2006.01.008](https://doi.org/10.1016/j.soildyn.2006.01.008).
- Toms, J., T. M. Müller, and B. Gurevich, 2007, Seismic attenuation in porous rocks with random patchy saturation: *Geophysical Prospecting*, **55**, 671–678, doi: [10.1111/j.1365-2478.2007.00644.x](https://doi.org/10.1111/j.1365-2478.2007.00644.x).
- Toms-Stewart, J., T. M. Müller, B. Gurevich, and L. Paterson, 2009, Statistical characterization of gas-patch distributions in partially saturated rocks: *Geophysics*, **74**, no. 2, WA51–WA64, doi: [10.1190/1.3073007](https://doi.org/10.1190/1.3073007).
- Vajdova, V., P. Baud, and T. F. Wong, 2004, Compaction, dilatancy, and failure in porous carbonate rocks: *Journal of Geophysical Research: Solid Earth*, **109**, B05204, doi: [10.1029/2003JB002508](https://doi.org/10.1029/2003JB002508).
- Wang, D. X., 2016, Study on the rock physics model of gas reservoirs in tight sandstone: *Chinese Journal of Geophysics*, **59**, 4603–4622, doi: [10.6038/cjg20161222](https://doi.org/10.6038/cjg20161222).
- White, J. E., 1975, Computed seismic speeds and attenuation in rocks with partial gas saturation: *Geophysics*, **40**, 224–232, doi: [10.1190/1.1440520](https://doi.org/10.1190/1.1440520).
- White, J. E., N. Mihailova, and F. Lyakhovitsky, 1975, Low-frequency seismic waves in fluid-saturated layered rocks. *The Journal of the Acoustical Society of America*, **57**, S30–S30, doi: [10.1121/1.1995164](https://doi.org/10.1121/1.1995164).
- Wu, C., J. Ba, J. M. Carcione, L. Y. Fu, E. M. Chesnokov, and L. Zhang, 2020, A squirt-flow theory to model wave anelasticity in rocks containing compliant microfractures: *Physics of the Earth and Planetary Interiors*, **301**, 106450, doi: [10.1016/j.pepi.2020.106450](https://doi.org/10.1016/j.pepi.2020.106450).
- Wu, C., J. Ba, X. Zhong, J. M. Carcione, L. Zhang, and C. Ruan, 2021, A new anelasticity model for wave propagation in partially saturated rocks: *Energies*, **14**, 7619, doi: [10.3390/en14227619](https://doi.org/10.3390/en14227619).
- Zhang, L., J. Ba, and J. M. Carcione, 2021, Wave propagation in infinituple-porosity media: *Journal of Geophysical Research: Solid Earth*, **126**, e2020JB021266, doi: [10.1029/2020JB021266](https://doi.org/10.1029/2020JB021266).
- Zhang, L., J. Ba, J. M. Carcione, and C. Wu, 2022, Seismic wave propagation in partially saturated rocks with a fractal distribution of fluid-patch size: *Journal of Geophysical Research: Solid Earth*, **127**, e2021JB023809, doi: [10.1029/2021JB023809](https://doi.org/10.1029/2021JB023809).
- Zhang, Y., O. Nishizawa, T. Kiyama, and Z. Xue, 2015, Saturation-path dependency of P-wave velocity and attenuation in sandstone saturated with CO₂ and brine revealed by simultaneous measurements of waveforms and X-ray computed tomography images: *Geophysics*, **80**, no. 4, D403–D415, doi: [10.1190/geo2014-0289.1](https://doi.org/10.1190/geo2014-0289.1).
- Zhu, W., P. Baud, and T. F. Wong, 2010, Micromechanics of cataclastic pore collapse in limestone: *Journal of Geophysical Research: Solid Earth*, **115**, B04405, doi: [10.1029/2009JB006610](https://doi.org/10.1029/2009JB006610).

Biographies and photographs of the authors are not available.